Fourth International Symposium on Marine Propulsors
smp'15, Austin, Texas, USA, June 2015
Workshop: Propeller Performance

Computational Analysis of Cavitating Marine Propeller Performance using OpenFOAM

Abolfazl Asnaghi, Andreas Feymark, Rickard E. Bensow

Department of Shipping and Marine Technology,
Chalmers University of Technology, Gothenburg, Sweden

ABSTRACT

In this paper, numerical results, based on implicit LES and transport equation mass transfer modelling approach, submitted to the Second International Workshop on Cavitating Propeller Performance at the Fourth International Symposium on Marine Propulsors (SMP'15) are presented. The numerical simulations are performed using OpenFOAM. The present work is focused on the second task of the workshop, *Propeller in oblique flow inside tunnel in wetted and cavitating conditions*. We summarise results from the three different operating conditions given in the task, where the experimental data of one condition is revealed, and the two other conditions are put forward as blind tests to workshop participants. For the condition where experimental data is known, we see good agreement for the forces in wetted conditions that slightly deteriorate in cavitating conditions. Cavitation extent is over predicted, where mid-span bubbly cavitation in the experiments is predicted as a sheet cavity; cavitation in the tip region does however seem reasonable. This is also likely the reason for the larger error in force prediction. A limited mesh resolution study has been performed.

Keywords

Cavitation, Numerical Simulation, OpenFOAM.

1 INTRODUCTION

A controllable pitch propeller with extensive experimental data is provided by SVA Potsdam to be considered for SMP'15 Workshop on Cavitation and Propeller Performance. The current work covers the performance prediction of the propeller in the cavitating conditions (Case 2) in three different operating conditions. The workshop is organized in a 'blind test' format where none of the participants knows the experiment results prior to the workshop.

The current numerical simulations have been conducted using a modified interPhaseChangeDyMFoam solver of OpenFOAM (OpenFOAM foundation). Implicit LES approach is adopted to account for turbulence (Bensow and Bark, 2010). The Schnerr-Sauer mass transfer model is employed to mimic the phase change between vapour and liquid (Schnerr and Sauer, 2001).

The presented results consist of simulations of three different operating conditions for wetted and cavitating flows, denoted as Case2.1, 2.2, and 2.3, see Table 1. For each of the operating conditions, the thrust and torque coefficients are presented. The effects of the mesh resolution, the inlet location and also the time discretization scheme on the numerical simulation are also investigated in this work and reported for Case2.1. The cavitation pattern at different blade positions for suction side and pressure side are presented. For Case2.1 that the experimental data are available the numerical results are analysed and compared with experiment.

2 Governing Equations

In the current study, the effective flow and each phase have been considered incompressible and isothermal which is a common engineering approach for cavitating flows. A mixture assumption is adopted using Transport Equation Modelling of volume fraction (TEM) for the phase distribution.

2.1 Mass and momentum equations

The conservation equations of mass and momentum for the effective fluid can be written as follow,

$$\frac{\partial \rho_m}{\partial t} + \frac{\partial \left(\rho_m u_i\right)}{\partial x_i} = 0 \tag{1}$$

$$\frac{\partial \left(\rho_m u_i\right)}{\partial t} + \frac{\partial \left(\rho_m u_i u_j\right)}{\partial x_j} = \frac{\tau_{ij}}{\partial x_j} + \rho_m g_i \tag{2}$$

The stress tensor in Newtonian fluids is conventionally written in the form of summation of pressure stress and shear stresses as follow.

$$\tau_{ij} = -p\delta_{ij} + S_{ij} - \frac{2}{3}\mu \frac{\partial u_m}{\partial x_m}\delta_{ij} \tag{3}$$

$$S_{ij} = 2\mu D_{ij} \tag{4}$$

In these equations, p is the static pressure, μ is the effective viscosity and S is the viscous stress tensor and D is the deformation rate tensor (symmetric part of the velocity strain), defined as $D_{ij} = \left(\partial u_i/\partial x_j + \partial u_j/\partial x_i\right)/2$.

2.2 Turbulence modelling

For turbulence modelling, implicit Large Eddy Simulation approach, ILES, is used. This turbulence model has been used and proved effective previously by the authors for simulation of the cavitating flows (Bensow and Bark, 2010), as well as for wetted flows.

Using the low pass filtering approach, the momentum equation in LES model can be written as Eq. (5).

$$\frac{\partial\left(\rho_m \overline{u_i}\right)}{\partial t} + \frac{\partial\left(\rho_m \overline{u_i u_j}\right)}{\partial x_j} = -\frac{\overline{p}}{\partial x_i} + \frac{\partial}{\partial x_j}\left(\overline{S}_{ij} - B_{ij}\right) + \rho_m g_i \tag{5}$$

The over bar denotes the low pass filtering quantities. In this equation, the subgrid stress tensor is $B_{ij} = \rho\left(\overline{u_i u_j} - \overline{u_i}\,\overline{u_j}\right)$.

In ILES approach no explicit model is applied for B, instead the numerical dissipation is considered enough to mimic the action of B (Bensow and Bark, 2010). Therefore, for momentum convection term, a relatively dissipative scheme should be used to provide appropriate numerical diffusion in the solution procedure.

2.3 Multiphase modelling

TEM, Transport Equation Model, is used in this study to model the transport of phases. In the TEM approach the spatial distribution of each phase is specified using a volume fraction function. Using the volume fraction, it is possible to calculate the mixture density and mixture viscosity based on the homogenous flow assumption.

$$\rho_m = \alpha_l \rho_l + (1-\alpha_l)\rho_v, \qquad \mu_m = \alpha_l \mu_l + (1-\alpha_l)\mu_v \tag{6}$$

$$\frac{\partial \alpha_l}{\partial t} + \frac{\partial\left(\alpha_l u_i\right)}{\partial x_i} = \frac{\dot{m}}{\rho_l} \tag{7}$$

In Eq. (7), which represents the transport equation of liquid volume fraction, the source term is the rate of phase change between vapour and liquid phases.

Based on the fluid properties and also the local flow properties, different models have been proposed to predict the cavitation phase change rate, $\dot{m}$ in the Eq. (7). In the current study, the mass transfer model proposed by Schnerr and Sauer is employed, Eq. (8), where average nucleus per liquid volume is considered constant and in this study equal to $n_0 = 10^8$, and the initial nuclei radius is $d_{Nuc} = 10^{-4}$ m.

$$\dot{m} = sign(P_{sat} - P)\frac{n_0}{1 + n_0 \frac{4}{3}\pi R^3} 4\pi R^2 \sqrt{\frac{2|P_{sat} - P|}{3\rho_l}} \tag{8}$$

Using the saturation pressure as the pressure threshold for phase change in the cavitating flows is based upon the liquid rupturing at the static or quasi-static conditions. In these conditions, the static pressure in the major part of the liquid is much larger than the viscous shear stresses. Although this estimation, using the saturation pressure as the pressure threshold, has been used widely in numerical simulation of cavitation, it does not take into account the effects of the shear stresses in the liquid rupturing and initiating phase change. In order to consider the viscous stresses, the eigenvalue of the stress tensor should be considered as the criteria on whether the fluid withstands rupturing or phase change. Here the modification proposed in Asnaghi et al. (2014) has been employed.

$$p_{threshold} = \mu\dot{\gamma} + p_{saturation} \tag{9}$$

$$\dot{\gamma} = \sqrt{2D_{ij}D_{ij}} \tag{10}$$

The added term is important if either shear strain rate or effective viscosity is large enough, and comparable with the static pressure value. For the flow around the foils, this is the case near the leading edge or during the collapse when the velocity variation is very high, and for the flow around the propellers this is the case both at the tip and leading edge regions.

2.4 Non-dimensional parameters

The definition of advance coefficient (J), cavitation number (σ_n), thrust coefficient (K_T) and torque coefficient (K_Q) are as follow,

$$J = V_A/\left(n \cdot D_p\right) \tag{11}$$

$$\sigma_n = \left(p - p_{sat}\right)/\left(0.5 \cdot \rho \cdot n^2 \cdot D_p^2\right) \tag{12}$$

$$K_{Tx} = T_x/\left(\rho \cdot n^2 \cdot D_p^4\right) \tag{13}$$

$$K_Q = Q/\left(\rho \cdot n^2 \cdot D_p^5\right) \tag{14}$$

where in these equations, V_A is the advance velocity (i.e. in this case the inlet velocity), n is the rotational speed of the propeller, p is the tunnel outlet pressure, T is the propeller thrust, and Q is the propeller torque.

3 Solution Procedure and Discretization

In order to solve the governing equations, OpenFOAM-2.3.x which is an open source CFD software package developed by OpenCFD Ltd at ESI Group and distributed by the OpenFOAM Foundation is used. In this software, the spatial discretization is performed using a cell centered co-located finite volume (FV) method for unstructured meshes with arbitrary cell-shapes, and a multi-step scheme is used for the time derivatives. The interPhaseChangeDyMFoam solver is employed to simulate the cavitation. The implicit LES model is implemented into the original code and in order to reduce the mesh resolution requirement for LES simulations near the walls, the Spalding wall model is employed to correct the turbulent viscosity at the first cell.

The PIMPLE algorithm is used to solve the coupling between the velocity and pressure. The residual of solving pressure and velocity in each iteration is set equal to 1e-6 for wetted flow and 1e-12 for cavitation simulation. A second order implicit time scheme (backward scheme) is used for time discretization. For one condition, the effects of using first order Euler scheme, often suggested sufficient when using small time steps, is also investigated and discussed.

A blending scheme of first order upwind and second order central difference schemes is used for the convective term. The constant of this blending is set equal to 0.2. All of the gradients have been corrected to consider non-orthogonality effects of neighbouring cells. For the volume fraction transport equation, first order upwind scheme is utilized.

In order to handle the rotation of the propeller, the computational domain is decomposed in two regions, the rotating region close to the propeller and the outer region, coupled via the standard sliding mesh implementation in OpenFOAM. The data across the regions are interpolated through the AMI boundaries in OpenFOAM.

4 Test Conditions

The propeller geometry and three different operating conditions are provided by SMP'15 workshop organisers. The propeller is a model scale, five bladed propeller with a diameter equal to 250 mm, Fig. 1.

The cavitation tests were conducted in the cavitation tunnel K 15 A of the SVA Potsdam. During testing the propeller was positioned according to the Fig. 2 with a 12° inclination of the propeller towards the inflow direction. In Table 1, the operating conditions are briefly presented.

Table 1: Operating conditions

Case	J	σ_n	V_{inlet} (m/s)	n (rev/sec)
2.1	1.019	2.024	5.095	20
2.2	1.269	1.424	6.345	20
2.3	1.408	2.0	7.04	20

5 RESULTS AND DISCUSSION

The numerical results consist of propeller performance (i.e. thrust and torque coefficients) predictions in the wetted and cavitating flows for three different operating conditions, described in Table 1. For the cavitating flows, the cavitation pattern at different blade positions are also plotted and investigated. The angular positions of the blades are described according to the right-handed rotation of the propeller with zero degree being equivalent to the 12 o'clock position.

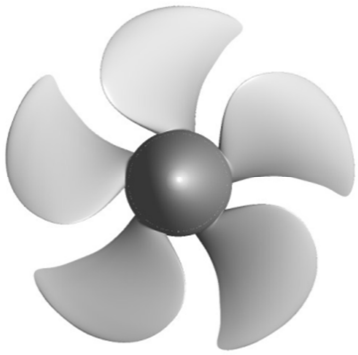

Figure 1: Propeller geometry

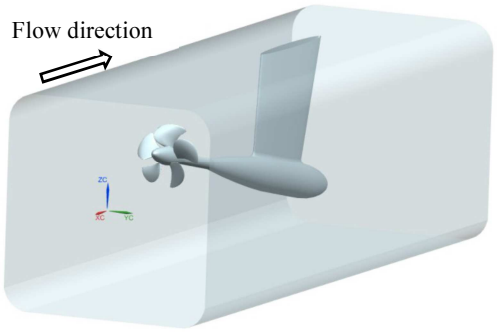

Figure 2: Test section

Since the experimental data are provided just for Case2.1, the numerical results are compared with the experimental data just for this case.

In order to elaborate the study, for the operating condition Case2.1, effects of using first order Euler time scheme, distance of the inlet boundary location relative to the propeller, and also mesh resolution are investigated and results are presented and compared with experimental data.

5.1 Boundary conditions

A summary of the numerical boundary setup is presented in Table 2. In order to reduce the requirement of mesh resolution near the tunnel wall, slip boundary condition is applied for the tunnel wall. The uniform inlet velocity and uniform outlet pressure are adopted to adjust the flow advance ratio and cavitation number.

5.2 Mesh specifications

The blades surface mesh consists of quad surfaces, which then have been extruded in the wall normal direction (y^+=10) to create prism cells (hexahedrals) in order to better capture the boundary layer over the blades. The rest of the domain is filled with unstructured tetrahedral cells. Since the flow has higher gradients near the leading and trailing edges and also near the tip region of the blades, the mesh has finer resolution at these areas. In order to limit the mesh size in a reasonable range, the mesh gets coarser by increasing distance from the blades.

Table 2: Numerical boundary setup

Boundary	Velocity	Pressure	nu_{Sgs}	Vapour (α)
Inlet	Fixed	Zero gradient	Zero gradient	Fixed
Outlet	Zero gradient	Fixed	Zero gradient	Zero gradient
Propeller surfaces	No-slip	Zero gradient	Wall model	Zero gradient
Tunnel wall	Slip	Zero gradient	Zero gradient	Zero gradient

In order to handle the rotation of the propeller, the computational domain is decomposed in two regions, the rotating region close to the propeller, and the stationary region where the total size of the mesh is around 4.7 M cells, called MeshI in this paper. For this mesh, the domain size has been kept the same as the geometry provided by the workshop committee.

In the provided geometry of the tunnel, the inlet is located almost in 2D upstream of the propeller. Since the inlet is relatively close to the propeller, it is possible that using uniform inflow as inlet velocity boundary condition affects the flow around the propeller (e.g. pressure distribution and cavitation pattern). Therefore, another mesh is also created where the inlet is moved 4D further upstream, MeshII in Fig. 3.

In order to investigate the effects of the mesh resolution on the results, MeshIII is created from MeshII where the prism cells around one blade are refined using refineMesh command in OpenFOAM. This command splits a hex cell into 2 cells in each direction. Therefore, the final cells are 8 times smaller than the original one. The final total cell size for this mesh is around 8.5 M cells. The blades surface mesh is presented in Fig. 4.

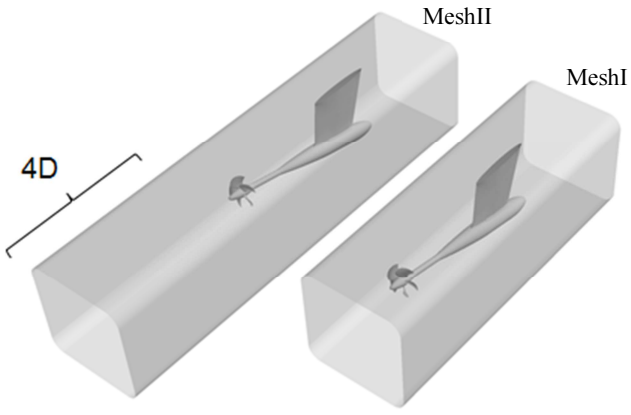

Figure 3: The inlet locations for MeshI and MeshII

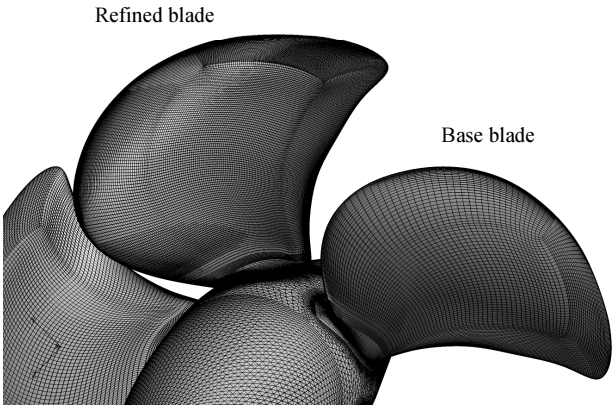

Figure 4: The blade surface mesh for MeshIII

5.3 Wetted flow results

In Table 3, the thrust and torque coefficients for the three different operating conditions are presented. Comparison between the experimental data and numerical results for Case2.1 shows that the obtained results have a good agreement with the experiment.

Table 3: Thrust and torque coefficients for wetted flow simulations

Operating conditions	Mesh	Time scheme	Method	K_{Tx}	$10K_Q$
Case2.1	------		Exp	0.397	1.02
	MeshI	backward	ILES	0.405	1.01
	MeshI	Euler	ILES	0.408	1.01
	MeshII	backward	ILES	0.404	1.00
	MeshIII	backward	ILES	0.406	1.01
Case2.2	MeshI	backward	ILES	0.262	0.72
Case2.3	MeshI	backward	ILES	0.181	0.55

5.4 Cavitating flow results

In Table 4, the thrust and torque coefficients for the three different operating conditions of cavitating flow are presented. For Case2.1, where the experimental data are available, comparison between numerical results and experimental data reveals that the comparison error is around 8% for K_Q and 4% for K_{Tx} prediction using backward scheme. However, the results related to Euler scheme show a severe over prediction of K_Q by 35%.

5.4.1 Case2.1

In Fig. 5, cavitation pattern for two iso-surfaces of alpha (40% and 60%) are presented for suction and pressure sides of the propeller. These results are related to the MeshI with backward time scheme. Note that we do not see any pressure side cavitation, but the image only reveals the extended sheet of the suction side.

Table 4: Thrust and torque coefficients for cavitating flow simulations

Operating conditions	Mesh	Time scheme	Method	K_{Tx}	$10K_Q$
Case2.1			Exp	0.36	0.94
	MeshI	backward	ILES	0.373	1.07
	MeshI	Euler	ILES	0.351	1.34
	MeshII	backward	ILES	0.374	1.05
	MeshIII	backward	ILES	0.375	1.04
Case2.2	MeshI	backward	ILES	0.196	0.73
Case2.3	MeshI	backward	ILES	0.157	0.53

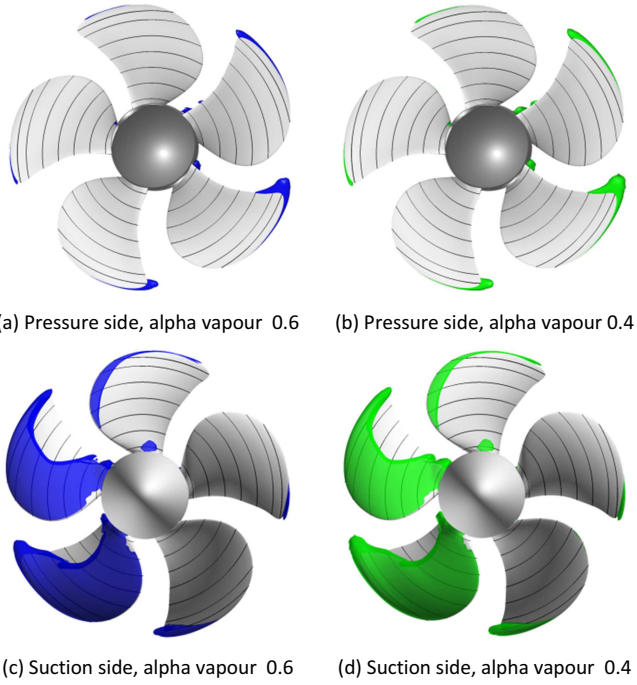

(a) Pressure side, alpha vapour 0.6 (b) Pressure side, alpha vapour 0.4

(c) Suction side, alpha vapour 0.6 (d) Suction side, alpha vapour 0.4

Figure 5: Case2.1, view along x-axis

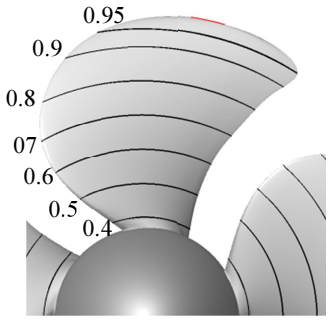

Figure 6: Description of radius ratio over the blade surface, view along x-axis

The lines on the surface of the blade represent the radius ratio, *r/R*, where *R* is the propeller radius and r is the distance from the centre of the propeller in the cylindrical coordinate system aligned with the propeller shaft, Fig. 6.

In Fig.7, the cavitation prediction for different settings and mesh resolutions are presented for Case2.1 where the vapour iso-surface is 60%.

For MeshIII, the picture is modified in a way that each blade position is replaced with the corresponding results of the blade having the refined mesh. Therefore, the picture somehow represents the results for an imaginary fully refined propeller.

Comparison between results of Fig. 7-c and Fig. 7-d will reveal the effects of mesh resolution on the cavitation prediction. From the results it can be deduced that the finer mesh is more capable of capturing and preserving the vortex rolled up into the blade tip region; note that the only the region around the blade is refined and not when the vortex has left the blade. From blade positions zero degree, it can be seen that finer mesh resolution was able to preserve the tip vortex cavitation longer, till the end of blade tip while in the coarser mesh the tip vortex cavitation is ended before reaching the blade tip. From the blade position 72 degree, it can be seen that in the finer mesh the vortex is rolled up earlier into blade tip region, and also from the blade position 216 degree, it can be seen that the preserved cavity is bigger than in the coarser mesh. These three main effects are highlighted by yellow ovals in the figures. We remark that the mesh refinement does not affect the over predicted mid radii sheet.

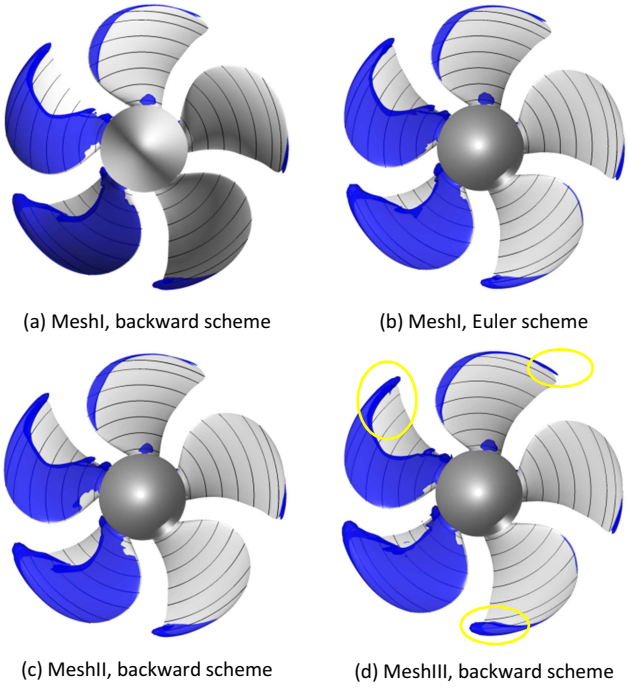

(a) MeshI, backward scheme (b) MeshI, Euler scheme

(c) MeshII, backward scheme (d) MeshIII, backward scheme

Figure 7: Case2.1, view along x-axis, Suction side, vapour iso-surface 0.6

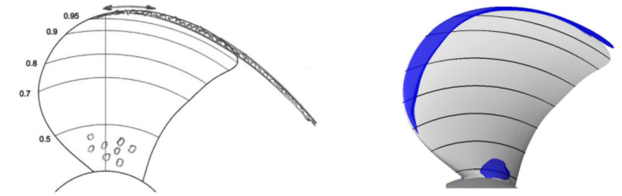

(a) Blade position zero degree

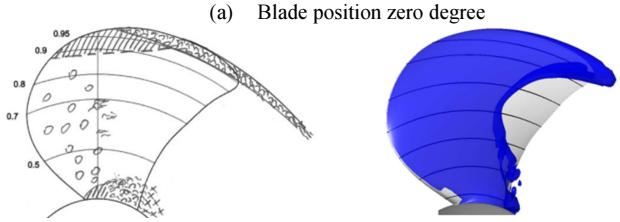

(b) Blade position 90 degree

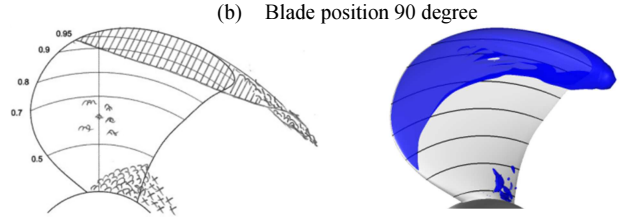

(c) Blade position 180 degree

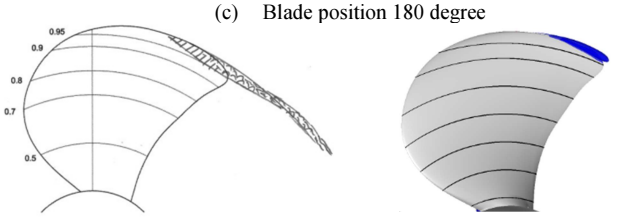

(d) Blade position 270 degree

Figure 8: Comparison between numerical results and experimental sketches for cavitation in Case2.1, view along x-axis, suction side, numerical results: MeshIII, vapour iso-surface: 0.6

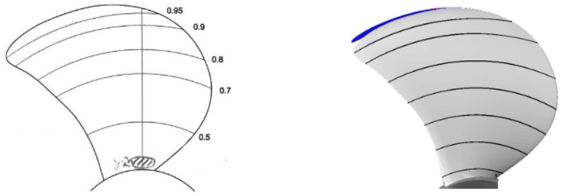

(a) Blade position zero degree

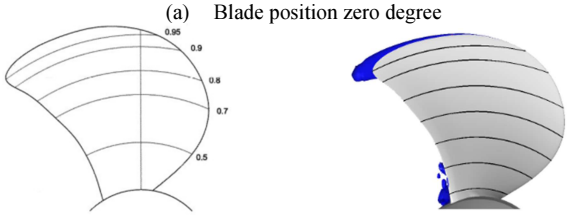

(b) Blade position 90 degree

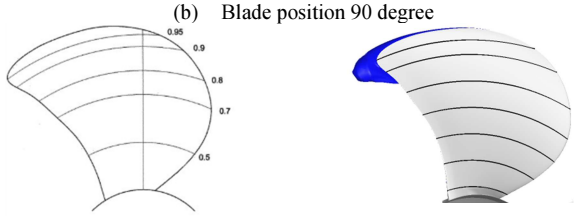

(c) Blade position 180 degree

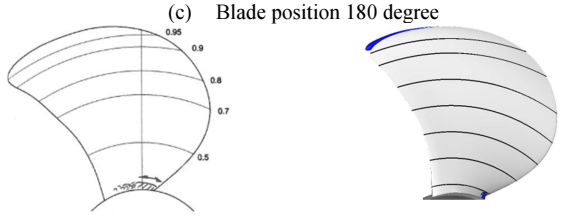

(d) Blade position 270 degree

Figure 9: Comparison between numerical results and experimental sketches for cavitation in Case2.1, view along x-axis, pressure side, numerical results: MeshIII, Vapour Iso-surface: 0.6

In Figs. 8 and 9, the cavitation predictions are compared with the experimental sketches for Case2.1 for the suction side and pressure side at different blade positions. As it is shown in Fig. 8, the general trend of the cavitation has been predicted reasonably well. The main difference between numerical results and the experimental data is related to the region with the bubbly cavitation pattern. In Fig.8-a, the bubbly root cavitation is predicted as sheet cavity, and in Fig.8-b the bubbly cavitation near the leading edge is predicted with the sheet leading edge cavitation. This sheet cavity then is attached to the near tip sheet cavity (radius 0.9) and covers almost all of the suction side of the blade. The type of bubble cavitation in the experiments indicates a blade pressure close to, or even below, vapour pressure. The modelling used here can not accommodate the growth of individual nuclei to this type of bubble cavitation, instead leading to this formation of a sheet over the leading half of the blade. The pressure side of the blade experiences root cavitation at blade positions of zero and 270 degrees during the experiment. The numerical simulation under predicts root cavitation at zero degree position, and 270 degree blade position.

In Fig. 10, the pressure coefficient of the wetted flow and also the vapour iso-surface 60% are presented for Case2.1. The pressure coefficient values, Fig. 10-a, are adjusted to show the values below C_p = -2, which represent regions with pressure lower than the saturation pressure.

As it is discussed before, the main discrepancy between numerical prediction of cavitation extent and the experimental observations is related to the prediction of leading edge sheet cavitation, e.g. at the blade positions 72 and 144 degrees in Fig. 10.

In the leading edge regions where the numerical prediction show pressure lower than the saturation pressure, the computational model will start to produce vapour. In the experiments, the formation of a sheet cavity depends as well on the nuclei content and nuclei residence time in the low pressure region. This is a modelling discrepancy between the numerical and experimental procedures.

Bubble cavitation is observed in the experiment to incept from the leading edge at these positions which suggests a blade pressure close to, or possibly even below, vapour pressure while the numerically predicted pressure at the leading edge is far lower than the saturation pressure in a considerable region. Without further experimental data,

clarifying the actual blade pressure, it's difficult to assess whether the difference in prediction is related to an error in the flow modelling, or if there are, e.g., geometrical differences between the tested and modelled propeller causing this deviation. However, it is also known that a laminar boundary layer can supress the cavitation inception even though pressure is far below the saturation pressure.

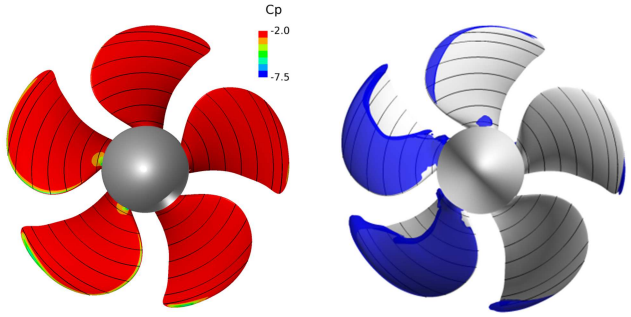

(a) Suction side, wetted flow, pressure coefficient

(b) Suction side, cavitating flow, alpha vapour 0.6

Figure 10: Case2.1, MeshI, backward scheme, view along x-axis

5.4.2 Case2.2

Cavitation prediction of Case2.2, presented in Fig. 11, shows cavitation appearances in both pressure side and suction side of the blade. It should be noted that the mesh is constructed in a way that has finer resolution in the suction side of the blades. As a result the cavitation is less resolved on the leading edge of the pressure side comparing to the suction side. The most pronounced feature is the leading edge cavitation which seems to start from the mid-chord of the blade on the suction side and then cavity extends till the trailing edge.

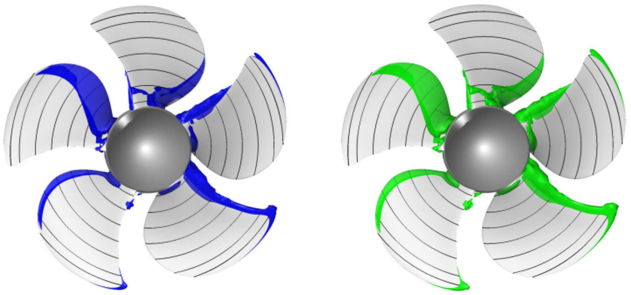

(a) Pressure side, alpha vapour 0.6

(b) Pressure side, alpha vapour 0.4

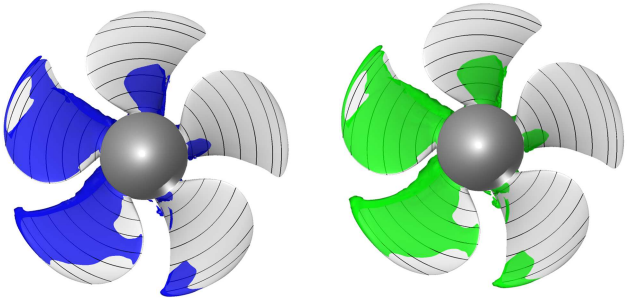

(c) Suction side, alpha vapour 0.6

(d) Suction side, alpha vapour 0.4

Figure 11: Case2.2, view along x-axis

5.4.3 Case2.3

In Fig. 12, cavitation prediction of Case2.3 is presented. The root cavitation is predicted for both suction and pressure sides of the blade at different positions. The leading edge cavitation is predicted for just the pressure side of the blade. At position 135 degree, tip cavitation is predicted for both sides of the blade.

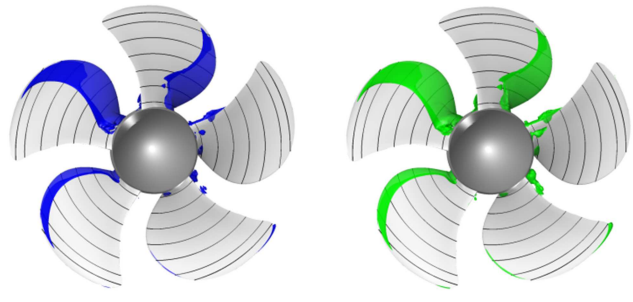

(a) Pressure side, alpha vapour 0.6

(b) Pressure side, alpha vapour 0.4

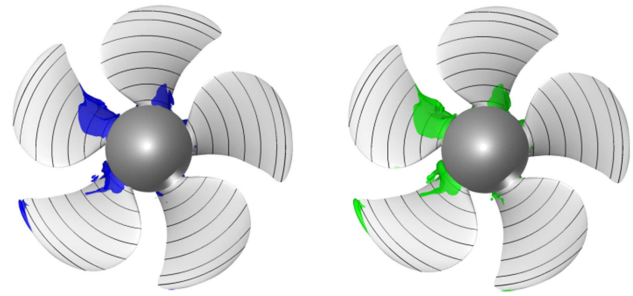

(c) Suction side, alpha vapour 0.6

(d) Suction side, alpha vapour 0.4

Figure 12: Case2.3, view along x-axis

6 CONCLUSION

Numerical simulations of cavitation of the Potsdam propeller test case (Case2) at three operating conditions are presented in this paper. For Case2.1 that the experimental data are available, results indicate that the employed numerical tool can predict the thrust and torque coefficients in the wetted and cavitating flows reasonably well. The cavitation simulation shows over prediction of the cavity size especially at the region that the bubbly cavitation is observed during the experiment.

ACKNOWLEDGMENTS

Financial support of this work has been provided by Rolls-Royce Marine through the University Technology Centre in Computational Hydrodynamics hosted at the Department of Shipping and Marine Technology, Chalmers. Computational resources have been provided by Chalmers Centre for Computational Science and Engineering, C3SE.

REFERENCES

Asnaghi, A., Feymark, A., and Bensow, R.E., (2014), "Shear Stress Effects in Cavitating Flows", 17th Numerical Towing Tank Symposium, 28-30 Sep., 2014, Marstrand, Sweden

Bensow, R.E. and Bark, G. (2010). "Implicit LES Predictions of The Cavitating Flow on a Propeller". J. Fluids Engineering 132.

Fourth International Symposium on Marine Propulsors & Second International Workshop on Cavitating Propeller Performance, May 31- June 4, 2015, Austin, Texas, USA, http://www.caee.utexas.edu/smp15/

OpenFOAM foundation, http://www.openfoam.com/, 28 April 2015

Propeller workshop smp'15, http://www.sva-potsdam.de/pptc_data_15.html, 28 April 2015

Schnerr, G. H. and Sauer J., (2001), "Physical and Numerical Modeling of Unsteady Cavitation Dynamics", In Fourth International Conference on Multiphase Flow, New Orleans, USA